


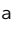



Cite this: *Sustainable Energy Fuels*,  
2022, 6, 3220

# Sb<sub>2</sub>S<sub>3</sub> solar cells with a cost-effective and dopant-free fluorene-based enamine as a hole transport material†

Nimish Juneja,<sup>a</sup> Sreekanth Mandati,<sup>b</sup> \*<sup>a</sup> Atanas Katerski,<sup>a</sup> Nicolae Spalatu,<sup>c</sup> <sup>a</sup> Sarune Daskeviciute-Geguziene,<sup>b</sup> Aivars Vembris,<sup>c</sup> Smagul Karazhanov,<sup>d</sup> Vytautas Getautis,<sup>b</sup> <sup>b</sup> Malle Krunkis,<sup>b</sup> <sup>a</sup> and Ilona Oja Acik <sup>a</sup>

Antimony sulphide (Sb<sub>2</sub>S<sub>3</sub>) is a promising candidate for semi-transparent and tandem solar cells owing to its suitable optoelectronic properties. However, the applications of Sb<sub>2</sub>S<sub>3</sub> solar cells are rather limited by their low power conversion efficiencies (PCEs) and use of expensive hole transport materials (HTMs). Furthermore, HTMs like P3HT exhibit parasitic absorption and hinder overall transparency of the devices. To circumvent these problems, V1236, a fluorene-based enamine is explored for the first time for Sb<sub>2</sub>S<sub>3</sub> solar cells, which is significantly cheaper, transparent, and does not require high temperature activation like P3HT. Solar cells are fabricated in the glass/FTO/TiO<sub>2</sub>/Sb<sub>2</sub>S<sub>3</sub>/HTM/Au configuration wherein TiO<sub>2</sub> and Sb<sub>2</sub>S<sub>3</sub> are deposited using ultrasonic spray pyrolysis and HTMs are spin coated. The concentration of V1236 is systematically varied and its impact on the Sb<sub>2</sub>S<sub>3</sub> device performance is investigated. The  $J_{SC}$  of the solar cells with V1236 is about 17% higher which is attributed to the better valence band edge alignment compared to P3HT. The EQE measurements show no parasitic absorption with V1236 while the optical studies show a larger bandgap for V1236 (2.6 eV) over P3HT (1.8 eV), indicating negligible loss of transparency. Furthermore, the overall transparency is increased by 20% for V1236 devices in comparison to P3HT devices while yielding better PCEs, demonstrating the efficacy of novel V1236 as an HTM for semi-transparent Sb<sub>2</sub>S<sub>3</sub> solar cells.

Received 15th March 2022  
Accepted 15th May 2022

DOI: 10.1039/d2se00356b

rsc.li/sustainable-energy

## 1 Introduction

Antimony chalcogenides are fast emerging as promising alternative light absorbing materials. Among them, Sb<sub>2</sub>S<sub>3</sub> is one of the most promising solar absorbers owing to its superior optoelectronic properties with an absorption coefficient of  $\approx 10^5 \text{ cm}^{-1}$  at 450 nm and a direct bandgap of  $\sim 1.8 \text{ eV}$ .<sup>1,2</sup> With a relatively wide bandgap, Sb<sub>2</sub>S<sub>3</sub> can be used either as an absorber material in single junction solar cells or as a light harvester in tandem cells.<sup>1,2</sup> Furthermore, Sb<sub>2</sub>S<sub>3</sub> solar cells are potential candidates for semi-transparent applications and have been under intense investigation for application in solar windows.<sup>3</sup> The constituent elements are non-toxic, earth abundant and cheaper, which makes the Sb<sub>2</sub>S<sub>3</sub> technology all

the more fascinating.<sup>1,4-6</sup> In recent years, with improvements in deposition techniques and interface engineering, Sb<sub>2</sub>S<sub>3</sub> solar cells have achieved a power conversion efficiency (PCE) of about 7.5%.<sup>7</sup> The deposition of Sb<sub>2</sub>S<sub>3</sub> absorbers by a variety of chemical and physical methods is reasonably well studied. Chemical bath deposition (CBD),<sup>6,7</sup> spin coating,<sup>8,9</sup> atomic layer deposition (ALD)<sup>10,11</sup> and chemical spray pyrolysis (CSP)<sup>5,12</sup> have been widely used for absorber fabrication. Among the low-cost solution-based methods, ultrasonic spray pyrolysis (USP) is a high throughput, area-scalable, and cost-effective deposition process, which is majorly used under ambient conditions. The efficacy of USP has been demonstrated by our group for the fabrication of Sb<sub>2</sub>S<sub>3</sub> thin film absorbers,<sup>3,5</sup> as well as for TiO<sub>2</sub> electron transport layers (ETLs).<sup>13,14</sup> The typical growth of Sb<sub>2</sub>S<sub>3</sub> by USP follows a two-step process involving the spray deposition of amorphous films followed by crystallization at elevated temperatures either in a vacuum or an inert atmosphere.<sup>3,5</sup> Physical methods for the deposition of Sb<sub>2</sub>S<sub>3</sub> absorbers include thermal evaporation,<sup>15,16</sup> magnetron sputtering<sup>1,17</sup> and closed space sublimation,<sup>18,19</sup> which resulted in efficiencies in the range of 3–6%.<sup>20,21</sup>

Conventional planar Sb<sub>2</sub>S<sub>3</sub> solar cells have utilized the glass/TCO/ETL/Sb<sub>2</sub>S<sub>3</sub>/HTM/metal configuration, wherein the transparent conducting oxide (TCO) and metal are the front and back

<sup>a</sup>Laboratory of Thin Film Chemical Technologies, Department of Materials and Environmental Technology, Tallinn University of Technology, Ehitajate tee 5, 19086 Tallinn, Estonia. E-mail: sreekanth.mandati@taltech.ee

<sup>b</sup>Department of Organic Chemistry, Kaunas University of Technology, Kaunas LT-50254, Lithuania

<sup>c</sup>Institute of Solid State Physics, University of Latvia, Kengaraga Str. 8, Riga, Latvia

<sup>d</sup>Institute for Energy Technology (IFE), P. O. Box 40, No 2027, Kjeller, Norway

† Electronic supplementary information (ESI) available: Synthesis procedure of the V1236 HTM, optical microscopy images of Sb<sub>2</sub>S<sub>3</sub>, transmittance and EQE curves. See <https://doi.org/10.1039/d2se00356b>



contacts. The electron transport layer (ETL) and hole transport material (HTMs) ferry the electrons and holes generated in the absorber to the contacts, respectively.<sup>3,5,22–26</sup> Indium tin oxide (ITO) and fluorine doped tin oxide (FTO) are commonly used TCOs.<sup>22,23,27</sup> For HTMs, several organic and inorganic materials are explored.<sup>15,28</sup> HTMs are an integral part of the solar cell structure and serve multiple tasks and are crucial to obtain high PCEs, especially for the semi-transparent device concept. HTMs ensure efficient extraction and transport of photogenerated holes to the contacts, prevent diffusion of metal to avoid direct contact with the absorber and suppress the recombination losses at the absorber–HTM interface.<sup>27</sup> HTMs must also possess high hole mobility, good thermal stability, high solubility in a suitable solvent, and appropriate band edge positions compatible with  $\text{Sb}_2\text{S}_3$ .<sup>27,29</sup> More importantly, they need to be transparent in the visible spectral region when used in semi-transparent solar cells and should be cost-effective. The most popular HTMs explored to date for  $\text{Sb}_2\text{S}_3$  solar cells are the organic-based P3HT (poly(3-hexylthiophene)),<sup>3,5,22,27</sup> spiro-OMeTAD (2,2',7,7'-tetrakis[*N,N*-di(4-methoxyphenyl)amino]-9,9'-spirobi-fluorene),<sup>24,25</sup> PEDOT:PSS (poly(3,4-ethylenedioxythiophene)-poly(styrenesulfonate))<sup>23</sup> and PCPDTBT (poly[2,6-(4,4-bis(2-ethylhexyl)-4*H*-cyclo-penta[2,1-*b*;3,4-*b'*]dithiophene)-*alt*-4,7-(2,1,3-benzothiadiazole)]).<sup>30</sup> Among inorganic materials,  $\text{NiO}_x$ ,<sup>31</sup>  $\text{V}_2\text{O}_5$ <sup>32</sup> and  $\text{CuSCN}:\text{KSCN}$ <sup>6</sup> have been reported as HTMs. For instance, Kim *et al.* have fabricated planar  $\text{Sb}_2\text{S}_3$  solar cells with spin coated PEDOT:PSS as the HTM wherein  $\text{Sb}_2\text{S}_3$  is deposited using CBD, and have obtained a PCE of 5.8%.<sup>23</sup> Zimmermann *et al.* used CBD for the deposition of the absorber and employed P3HT as the HTM where the impact of P3HT thickness on solar cell performance has been investigated resulting in a PCE of 4.1%.<sup>27</sup> You *et al.* used spin coating for deposition of  $\text{Sb}_2\text{S}_3$  and P3HT to fabricate solar cells with a PCE of 2.3%.<sup>22</sup> On a similar note, spiro-OMeTAD has also been used as an HTM for  $\text{Sb}_2\text{S}_3$  solar cells. Zhang *et al.* have used CBD to deposit  $\text{Sb}_2\text{S}_3$  with spiro-OMeTAD as the HTM and have reported an efficiency of 5.5%.<sup>24</sup> Chen *et al.* have adopted spin coating for  $\text{Sb}_2\text{S}_3$  deposition with spiro-OMeTAD as the HTM and demonstrated a PCE of 5.2%.<sup>25</sup> Choi *et al.* have deposited  $\text{Sb}_2\text{S}_3$  using CBD and have employed a combination of PCPDTBT and PEDOT:PSS as the HTM and fabricated solar cells (FTO/mp-TiO<sub>2</sub>/Sb<sub>2</sub>S<sub>3</sub>/PCPDTBT/PEDOT:PSS/Au) with a PCE of 7.5%, which remains the highest to date.<sup>7</sup> However, despite the successful demonstration of conventionally used HTMs like P3HT, spiro-OMeTAD, PCPDTBT, *etc.*, the high manufacturing costs of these materials coupled with low yields pose limitations on the commercial maturity of  $\text{Sb}_2\text{S}_3$  solar cells.<sup>33</sup> Furthermore, P3HT requires an additional activation step at temperatures around 170 °C.<sup>3,5</sup> Also, a similar bandgap value of P3HT (1.8 eV)<sup>3</sup> to that of  $\text{Sb}_2\text{S}_3$  (1.7 eV)<sup>5</sup> coupled with the parasitic absorption losses limits the overall transparency of solar cells.<sup>34</sup>

Considering the aforementioned HTM related drawbacks, this study aims to fabricate  $\text{Sb}_2\text{S}_3$  semi-transparent solar cells employing a fluorene-based enamine – V1236 (*N*<sup>2</sup>,*N*<sup>2</sup>,*N*<sup>7</sup>,*N*<sup>7</sup>-tetrakis[2,2-bis(4-methoxyphenyl)viny]-9,9-dihexyl-9*H*-fluorene-2,7-diamine) as an HTM for the first time. V1236 has been investigated as a dopant-free HTM in perovskite solar cells

yielding an efficiency of 17.1%.<sup>34</sup> V1236 possesses a band gap of 2.6 eV and a hole mobility of  $\approx 2.6 \times 10^{-4} \text{ cm}^2 \text{ V}^{-1} \text{ s}^{-1}$ .<sup>34</sup> Owing to its largely simplified synthesis process and high yield, the estimated synthesis cost of V1236 is  $\sim 17 \text{ € per g}$  (Table S1†), which is considerably cheaper than those of conventional HTMs like spiro-OMeTAD ( $\sim 92 \text{ € per g}$ )<sup>35</sup> and P3HT ( $\sim 45 \text{ € per g}$ ).<sup>36</sup> The present study focuses on validating the use of cost-effective V1236 as an HTM by demonstrating the successful fabrication of planar  $\text{Sb}_2\text{S}_3$  solar cells (glass/FTO/TiO<sub>2</sub>/Sb<sub>2</sub>S<sub>3</sub>/HTM/Au), wherein TiO<sub>2</sub> and Sb<sub>2</sub>S<sub>3</sub> layers are deposited using ultrasonic spray pyrolysis. For a fair comparison, the conventionally used P3HT is also employed and both the HTMs are spin coated. The solar cell devices with optimized V1236 and P3HT have resulted in similar efficiencies. Insights from band alignment reveal that V1236 serves as a better HTM due to its better LUMO level alignment with the conduction band edge of  $\text{Sb}_2\text{S}_3$  compared to P3HT. Additionally, the device stack from V1236 devoid of metal contact exhibits an increase in average visible transmittance (AVT) in the visible region over P3HT devices, demonstrating the efficacy of V1236 as an HTM in semi-transparent  $\text{Sb}_2\text{S}_3$  solar cells.

## 2 Experimental

### 2.1 Materials

FTO substrate ( $7 \Omega \square^{-1}$ ), titanium(IV) tetraisopropoxide (TTIP) – 99 wt% (Acros Organics), acetylacetone – 99 wt% (Acros Organics), ethanol – 96.6 vol% (Estonian Spirit), methanol – 99.9 vol% (Sigma-Aldrich), antimony trichloride – 99.99 wt% (Sigma-Aldrich), thiourea – 99 wt% (Sigma-Aldrich), chlorobenzene – 99.5 vol% (Sigma-Aldrich), poly(3-hexyl-thiophene-2,5-diyl) (P3HT) – 100 kDa, >90% regioregular (Sigma-Aldrich) and *N*<sup>2</sup>,*N*<sup>2</sup>,*N*<sup>7</sup>,*N*<sup>7</sup>-tetrakis[2,2-bis(4-methoxyphenyl)viny]-9,9-dihexyl-9*H*-fluorene-2,7-diamine (V1236). The materials are used as received. The chemical structures of V1236 and P3HT are shown in Fig. 1.

### 2.2 Methods

**2.2.1 Fabrication of solar cells.** The typical procedure adopted for the fabrication of  $\text{Sb}_2\text{S}_3$  solar cells is shown as a schematic in Fig. 2a and the device configuration is depicted in Fig. 2b. The glass/FTO substrates (25 mm × 25 mm) were rinsed thoroughly with deionized water, ethanol and methanol

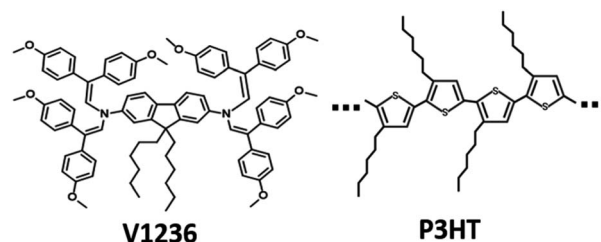


Fig. 1 *N*<sup>2</sup>,*N*<sup>2</sup>,*N*<sup>7</sup>,*N*<sup>7</sup>-Tetrakis[2,2-bis(4-methoxyphenyl)viny]-9,9-dihexyl-9*H*-fluorene-2,7-diamine (V1236) and poly(3-hexylthiophene-2,5-diyl) (P3HT).



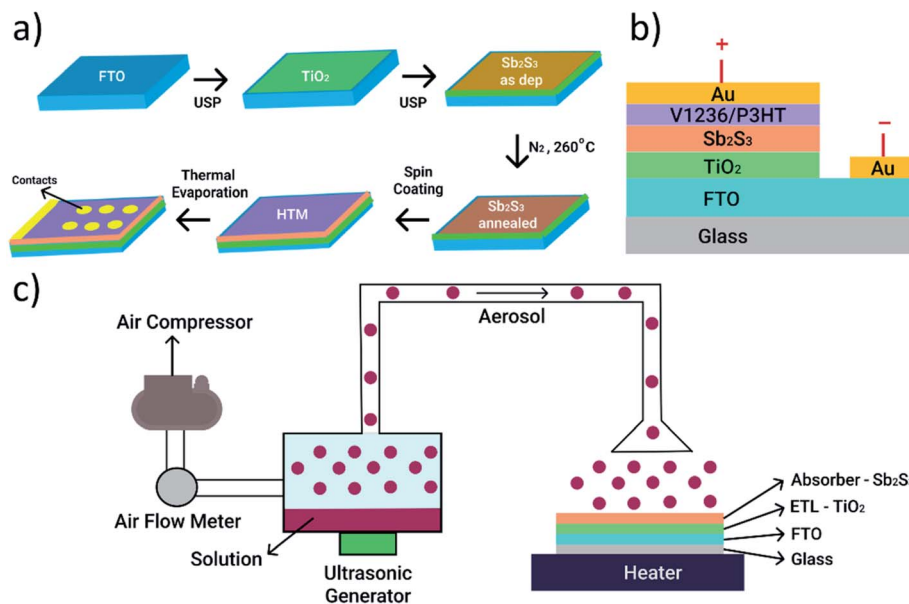


Fig. 2 (a) Schematic of the procedure adopted for the fabrication of Sb<sub>2</sub>S<sub>3</sub> solar cells, (b) Sb<sub>2</sub>S<sub>3</sub> solar cell configuration and (c) schematic of ultrasonic spray pyrolysis (USP) deposition.

followed by cleaning in boiled deionized water for 15 min and were dried with nitrogen prior to deposition. The TiO<sub>2</sub> precursor was prepared by mixing 0.2 M TTIP with 0.2 M acetylacetonate in ethanol. The TiO<sub>2</sub> electron transport layer (ETL) and Sb<sub>2</sub>S<sub>3</sub> absorber were deposited using an indigenously developed and scalable ultrasonic spray pyrolysis technique (USP) as shown in the schematic in Fig. 2c. The USP process is a conventional approach used for the fabrication of semiconducting absorbers. The typical process involves the generation of an aerosol from the precursor solution using an ultrasonic generator, and the aerosol is carried to the substrate surface using a carrier gas, which is compressed air. Furthermore, a director gas, also compressed air, is used to direct the aerosol onto the substrate surface, which is kept on a hot plate. Typically, the director gas nozzle moves in the *x*-*y* plane which covers the substrate for uniform coating. Each *x* and *y*-directional movement is termed a meander and a set of meanders covering the entire substrate is a cycle. The TiO<sub>2</sub> ETLs were sprayed with 8 meanders and for 75 cycles, which accounted for a sprayed solution of ≈ 80 ml and a deposition time of ≈ 35 min. A carrier gas flow rate of 7.5 l min<sup>-1</sup> was used, with a spray rate of 2.5 ml min<sup>-1</sup> while the substrate was kept at 340 °C. The as-deposited TiO<sub>2</sub> samples were annealed on a hot plate at 450 °C for 30 min in air. For Sb<sub>2</sub>S<sub>3</sub>, 60 mM of antimony chloride (SbCl<sub>3</sub>) was mixed with 180 mM of thiourea in methanol. A similar USP process was adopted for Sb<sub>2</sub>S<sub>3</sub> where the substrate temperature is 200 °C with the carrier gas flow rate being 2.5 l min<sup>-1</sup>. The same 8-meander approach is followed for a total of 40 cycles utilizing a precursor of ≈ 60 ml and a deposition time of ≈ 30 min, which resulted in a spray rate of 1.5 ml min<sup>-1</sup>. The as-deposited Sb<sub>2</sub>S<sub>3</sub> thin films on glass/FTO/TiO<sub>2</sub> substrates were then annealed at 250 °C for 5 min in a N<sub>2</sub> atmosphere. To complete the fabrication of solar cells, V1236 and P3HT were spin coated

from their respective precursors dissolved in chlorobenzene. The detailed synthesis process of V1236 is shown in the ESI and the materials are listed in Table S1.† While the concentration of V1236 was systematically varied to obtain the optimal value, the P3HT concentration was 1 wt%, which was conventionally used. It may be noted that after the spin coating of P3HT, the samples were heat treated in a vacuum at 170 °C for 5 min for activation of P3HT whereas no such step was employed for V1236. Finally, Au was thermally evaporated as the top contact with the active area of final solar cells being 7.06 mm<sup>2</sup>.

**2.2.2 Characterization.** The structure and phase constitution of the as-deposited and annealed Sb<sub>2</sub>S<sub>3</sub> films were characterized by X-ray diffraction (XRD) and spectra were collected using a Rigaku Ultima IV instrument with a Cu K<sub>α</sub> source ( $\lambda = 1.5406 \text{ \AA}$ ) in a  $2\theta$  range of 10–80° at a step size of 0.02°. Micro-Raman spectra were collected at room temperature using a Horiba LabRam HR 800 in the backscattering mode. The He-Ne laser intensity was attenuated to 143 μW μm<sup>-2</sup> over a focal area of  $\varnothing 5 \text{ μm}$  with a wavelength of 532 nm. Surface and cross-sectional morphologies of the layers were recorded using a Zeiss HR FESEM Ultra 55 (SEM) at an electron beam accelerating voltage of 4 kV. The elemental composition of the films was determined by energy dispersive X-ray spectroscopy (EDX) using a Bruker spectrometer with an ESPRIT 1.8 system at an accelerating voltage of 7 kV. Optical total transmittance and total reflectance spectra of the functional layers (FTO, TiO<sub>2</sub>, Sb<sub>2</sub>S<sub>3</sub>, P3HT and V1236) and the devices were measured in the 250–1100 nm range with reference to air using a Jasco V-670 ultraviolet-visible spectrophotometer (UV-VIS) equipped with a 40 mm integrating sphere.

The work function of Au contacts was measured using a Kelvin probe. To ascertain the band alignment, the ionization potential and electron affinities of the functional layers were



determined by the photoelectron emission spectroscopy method, which measures the dependence of the photoelectron emission current on the photon energy. The electron affinity (LUMO) is calculated as a difference between the ionization energy and photoconductivity threshold energy.<sup>37</sup> Current-voltage ( $I$ - $V$ ) characteristics of the solar cells were measured using a Wavelabs LS-2 LED solar simulator with an AM1.5G (100 mW cm<sup>-2</sup>) light source. External quantum efficiency (EQE) spectra were recorded using a Newport 69911 system with a 300 W Xenon lamp.

### 3 Results and discussion

The as-deposited and annealed Sb<sub>2</sub>S<sub>3</sub> films are characterized to ascertain the quality of films prior to their application in solar cells. XRD patterns of the as-deposited and annealed Sb<sub>2</sub>S<sub>3</sub> films deposited on the glass/FTO/TiO<sub>2</sub> substrate are shown in Fig. 3a. The pattern of the sample with the as-deposited Sb<sub>2</sub>S<sub>3</sub> films shows peaks belonging to FTO and anatase TiO<sub>2</sub> underlayers. In contrast, the annealed films show sharp intense peaks at  $2\theta$  of 15.9, 17.8, 29.2 and 30.5°, which are characteristic of the orthorhombic stibnite structure of Sb<sub>2</sub>S<sub>3</sub> (ICDD PDF 01-075-4013).<sup>3,5</sup> XRD data suggest that the as-deposited films are amorphous in nature and annealing induces crystallization. Additionally, no peaks corresponding to Sb<sub>2</sub>O<sub>3</sub> are detected, which are otherwise present at  $2\theta$  of 13.6 and 27.5°,<sup>3,5</sup> indicating that the annealed Sb<sub>2</sub>S<sub>3</sub> films are of high quality, and devoid of impurities and undesired phases such as oxides. To further

verify the crystallinity and phase of Sb<sub>2</sub>S<sub>3</sub>, the as-deposited and annealed films are characterized using Raman spectroscopy and the recorded spectra are shown in Fig. 3b. As revealed in the spectra, a wide Raman band centred at around 300 cm<sup>-1</sup> is detected in the sample with as-deposited films, which is characteristic of amorphous Sb<sub>2</sub>S<sub>3</sub>.<sup>3</sup> The patterns collected from annealed samples show several sharp peaks characteristic of orthorhombic Sb<sub>2</sub>S<sub>3</sub> at 128, 155, 188, 236, 280, 302, and 312 cm<sup>-1</sup>, which agree with previous reports.<sup>3,5</sup> XRD and Raman analyses corroborate each other to affirm the formation of amorphous and crystalline stibnite phases in as-deposited and annealed Sb<sub>2</sub>S<sub>3</sub> films, respectively, and have further confirmed the presence of single phase Sb<sub>2</sub>S<sub>3</sub> without any secondary phases. The surfaces of the as-deposited and annealed Sb<sub>2</sub>S<sub>3</sub> films are analysed using optical microscopy and the relevant images are shown in Fig. S1.†

The images clearly reveal that the surface of the substrates is conformally covered with amorphous Sb<sub>2</sub>S<sub>3</sub> films and the annealed films show a grain structure. Annealing of Sb<sub>2</sub>S<sub>3</sub> films has produced a visual colour change with the as-deposited films turning from orange to dark brown upon annealing (see Fig. S2.†). The elemental composition of the as-deposited and annealed Sb<sub>2</sub>S<sub>3</sub> films, determined using energy dispersive X-ray spectroscopy (EDS), shows an atomic ratio of 1.3 for S/Sb. The optical properties of the samples with the as-deposited and annealed Sb<sub>2</sub>S<sub>3</sub> thin films are analysed using UV-Vis-NIR absorption spectroscopy and the corresponding absorbance vs. wavelength curves are shown in Fig. 3c. The spectra reveal

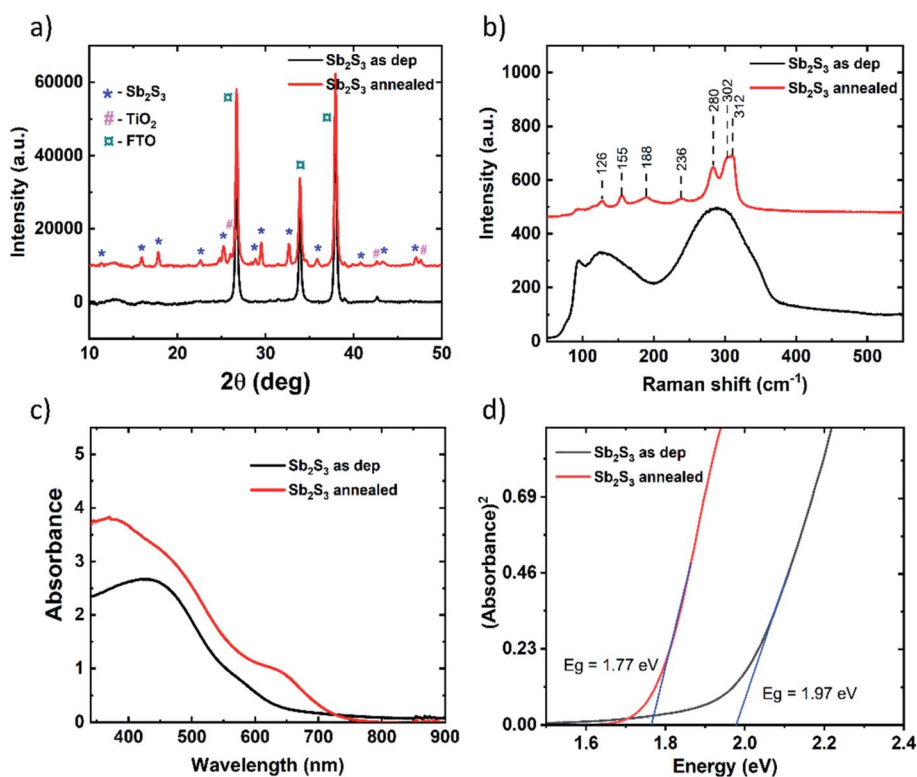


Fig. 3 (a) XRD patterns, (b) Raman spectra, (c) absorption spectra and (d) Tauc plots of as-deposited and annealed Sb<sub>2</sub>S<sub>3</sub> films. Substrate: glass/FTO/TiO<sub>2</sub>.



that the absorption is stronger in annealed  $\text{Sb}_2\text{S}_3$  films with a sharper absorption edge (around 700 nm) compared to amorphous films (around 650 nm). The optical band gap ( $E_g$ ) of amorphous and crystalline  $\text{Sb}_2\text{S}_3$  absorbers is determined using Tauc plots, as shown in Fig. 3d. The allowed band-to-band transitions are considered to be direct in nature while determining the bandgap. The bandgap values of amorphous and crystallized  $\text{Sb}_2\text{S}_3$  absorbers are inferred to be 2.1 and 1.8 eV, respectively, which agree well with previously reported values.<sup>3,5</sup> The morphological, compositional, structural and optical analyses of annealed  $\text{Sb}_2\text{S}_3$  films indicate that the absorber shows conformal coverage on the  $\text{TiO}_2$  layer, a single stibnite phase and a suitable direct bandgap as desired for solar cell applications. On the crystallized  $\text{Sb}_2\text{S}_3$  absorber, V1236 and P3HT are spin coated followed by the thermal evaporation of Au to complete the solar cell fabrication. The detailed synthesis procedure and materials adopted for V1236 are shown in the ESI.† The NMR and mass spectra of intermediate compounds during synthesis and the final V1236 are shown in Fig. S3 and S4,† respectively.

The current density–voltage ( $J$ – $V$ ) characteristics of the devices are measured under one sun illumination (AM 1.5G) and the  $J$ – $V$  curves of the champion cells for each device are shown in Fig. 4 and the corresponding photovoltaic parameters are summarized in Table 1. Primarily, solar cells are prepared using V1236 with a concentration of 15 mM as has been

previously used to fabricate perovskite solar cells.<sup>29</sup> However, the  $\text{Sb}_2\text{S}_3$  solar cells with 15 mM V1236 exhibit a low power conversion efficiency (PCE) of 0.1%, with an open circuit voltage ( $V_{\text{OC}}$ ) of 566 mV, a short-circuit current density ( $J_{\text{SC}}$ ) of 0.87  $\text{mA cm}^{-2}$ , and a fill factor (FF) of 0.15. While the reasonable  $V_{\text{OC}}$  value indicates the formation of the desired p–n junction, the devices hardly have yielded any  $J_{\text{SC}}$ . The layer thickness of 15 mM V1236 is estimated to be around 140 nm and the resulting series resistance ( $R_s$ ) of the device is estimated to be 17.2  $\Omega \text{ cm}^2$ . The extremely low  $J_{\text{SC}}$  of the solar cell could be attributed to the larger series resistance, which also results in a very low FF. To solve this issue, a series of experiments are carried out where the concentration of V1236 has been systematically reduced (4 $\times$ , 8 $\times$ , 16 $\times$  and 32 $\times$ ). The resulting concentrations of 4 mM, 2 mM, 1 mM and 0.5 mM are used for the HTM layer in the fabrication of solar cells. Fig. 4a shows the  $J$ – $V$  characteristics of solar cells with varied V1236 concentrations. As seen from Fig. 4a and Table 1, the concentration dilution has resulted in a considerable increase in PCE particularly arising from significantly higher  $J_{\text{SC}}$  compared to that of the 15 mM case. The highest PCE of 3.9% is obtained for 2 mM V1236 where the  $J_{\text{SC}}$  is 13.8  $\text{mA cm}^{-2}$ ,  $V_{\text{OC}}$  is 610 mV, and FF is 0.46. However, a further dilution in concentration has decreased the PCE, which is majorly affected by the decrease in  $V_{\text{OC}}$ . This could be attributed to a plausibly very thin V1236 film owing to the low concentration which may not be enough for

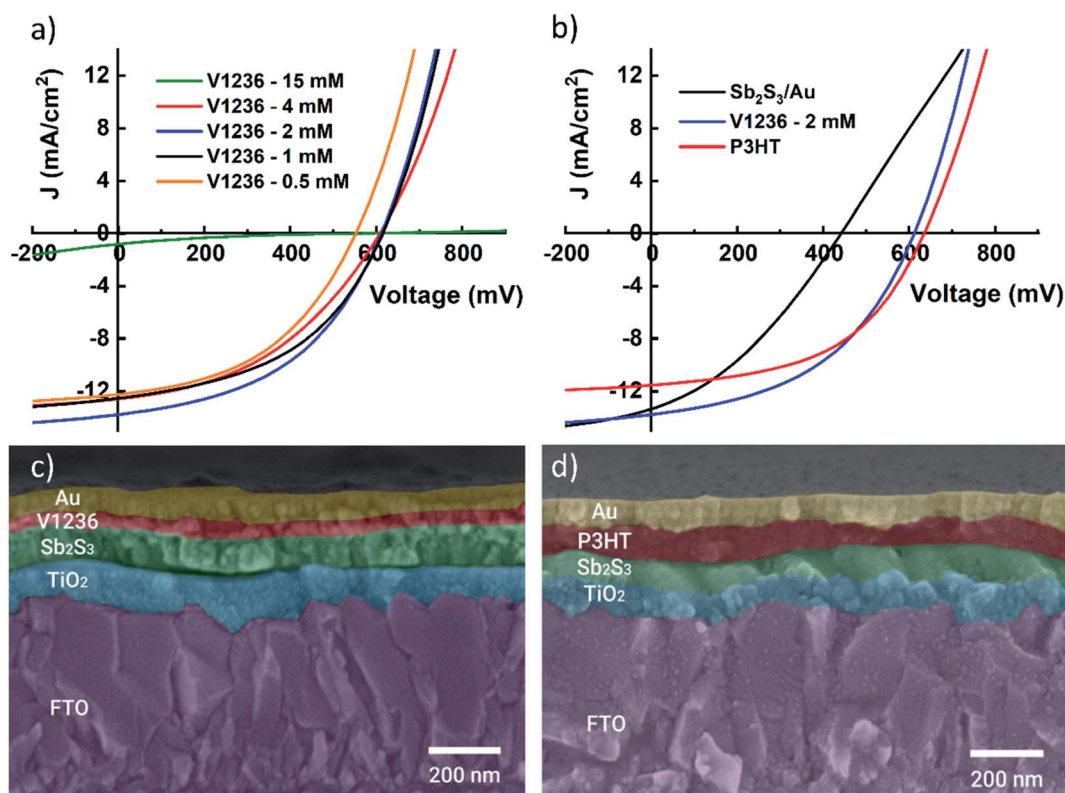


Fig. 4  $J$ – $V$  curves of the champion  $\text{Sb}_2\text{S}_3$  solar cells with (a) different concentrations of V1236 as the HTM. (b) Comparison of cells without an HTM and with optimized V1236 and P3HT. (c) and (d) Cross-sectional images of  $\text{Sb}_2\text{S}_3$  solar cells with optimized V1236 and P3HT as HTMs. Structure: glass/FTO/ $\text{TiO}_2$ / $\text{Sb}_2\text{S}_3$ /HTM/Au.



Table 1 Device parameters of Sb<sub>2</sub>S<sub>3</sub> solar cells without and with V1236 and P3HT HTMs

Sample	HTM conc. (mM)	V <sub>OC</sub> (mV)	J <sub>SC</sub> (mA cm <sup>-2</sup> )	FF (%)	PCE (%)	R <sub>S</sub> (Ω cm <sup>2</sup> )
Sb <sub>2</sub> S <sub>3</sub> /Au	No HTM	440	13.2	34	2.0	4.7
P3HT	1 wt%	634	11.5	50	3.7	3.1
V1236	15	566	0.9	15	0.1	17.2
V1236	4	608	12.5	42	3.2	0.7
V1236	2	612	13.8	46	3.9	0.6
V1236	1	614	12.5	46	3.6	0.5
V1236	0.5	552	12.2	45	3.0	0.4

the complete coverage of the underlying Sb<sub>2</sub>S<sub>3</sub> absorber. The layer thickness measured in the case of V1236 with 2 mM concentration is found to be ≈ 20 nm. A positive correlation is found between the concentration of V1236 and its thickness. As the concentration of V1236 decreases from 15 mM to 2 mM, the thickness decreases from approximately 140 nm to 20 nm. A decrease in the concentration of V1236, resulting in thinner films, has also led to a decrease in R<sub>S</sub>. Furthermore, for a fair evaluation of V1236 as an HTM, optimized solar cells with 2 mM concentration are compared with the devices made using P3HT as an HTM. The concentration of P3HT (0.5, 1 and 2 wt%) has been optimized as shown in Fig. S5,† which shows that solar cells with 1 wt% P3HT have yielded the highest PCE and are therefore used as the reference. The summarized device parameters from *JV* curves are shown in Table S2.† The *J-V* curves of solar cells with optimized V1236 and P3HT are compared as shown in Fig. 4b, which indicates almost comparable efficiencies, demonstrating the efficacy of V1236 as an HTM for Sb<sub>2</sub>S<sub>3</sub> solar cells. Furthermore, to understand the impact of HTMs as such, reference devices are made without HTMs, and have yielded a PCE of 2.0% with a lower V<sub>OC</sub> and FF. This fact affirms the need for HTMs in Sb<sub>2</sub>S<sub>3</sub> solar cells to obtain a higher V<sub>OC</sub> and hence, efficiency. In addition, to investigate any plausible hysteresis in devices, the forward and reverse *J-V* characteristics of Sb<sub>2</sub>S<sub>3</sub> solar cells with V1236 and P3HT as HTMs are measured and the plots are shown in Fig. S6.† The *J-V* curves in forward and reverse directions are almost identical and the calculated hysteresis index (HI) values in both the cases are <0.05 indicating negligible hysteresis in Sb<sub>2</sub>S<sub>3</sub> solar cells with both HTMs.

Cross-sectional images of solar cell stacks with optimized V1236 and P3HT are shown in Fig. 4c and d, respectively. The thickness of TiO<sub>2</sub> and Sb<sub>2</sub>S<sub>3</sub> is almost identical in both cases (≈ 90 nm) while V1236 is a considerably thinner layer (≈ 20 nm) compared to the P3HT layer (≈ 100 nm). It is important to note that the V1236 and P3HT are independently optimized for Sb<sub>2</sub>S<sub>3</sub> solar cells leading to higher efficiency, which shows that thinner V1236 is sufficient for obtaining similar efficiencies compared to a reasonably thicker P3HT. Therefore, irrespective of their thickness, the optimized V1236- and P3HT-based solar cells are further characterized and compared for band energetics, quantum efficiency, and overall transparency. The reproducibility of semi-transparent solar cells with V1236 and P3HT HTMs is compared with the box plots as shown in Fig. 5. The

spread is not only reasonably small but also almost identical for both the cases and for all the device parameters (V<sub>OC</sub>, J<sub>SC</sub>, FF and PCE), indicating the good reproducibility of solar cells.

Since V1236 is explored as an HTM for Sb<sub>2</sub>S<sub>3</sub> solar cells for the first time, it is imperative to understand the band edge positions of this material with respect to the absorber for a better understanding of device physics. It is well known that photogenerated electrons in the absorber flow towards the ETL (TiO<sub>2</sub>) and the holes towards the HTM. The energy levels at the Sb<sub>2</sub>S<sub>3</sub>/HTM interface have a strong effect on the hole extraction process. A staggered-gap heterointerface can benefit the process greatly and also prevent the electrons from passing to the HTM layer. The typical curves and the estimation of ionization energy for the V1236 HTM are shown in Fig. S7.† Fig. 6 shows the band energy diagram of solar cells with V1236 and P3HT. The energy levels of FTO, TiO<sub>2</sub>, Sb<sub>2</sub>S<sub>3</sub>, P3HT and V1236 are obtained from photoemission spectroscopy and intrinsic photoconductivity measurements. As clearly revealed in the figure, the HOMO of V1236 (-5.0 eV) is in closer proximity than P3HT (-4.6 eV) to the valence band edge of Sb<sub>2</sub>S<sub>3</sub> (-5.1). This could explain the enhanced performance of V1236 over P3HT due to better hole transport at the absorber-V1236 interface. An interesting observation from Table 1 is that devices with V1236 exhibit a slightly lower V<sub>OC</sub> than P3HT despite its deeper HOMO level. It may be noted that the observed difference (≈ 20 mV) in the present study is not significantly large. It is observed that the thickness of V1236 (≈ 20 nm) is considerably smaller than that of P3HT (≈ 100 nm) indicating a difference in the interface across Sb<sub>2</sub>S<sub>3</sub>/HTM/Au, which may also affect the V<sub>OC</sub>. In addition, the V<sub>OC</sub> of the device depends on other parameters like recombination at the absorber-HTM interface, the defects in the absorber, *etc.*, which necessitates deeper analysis like conducting transient photovoltage measurements to analyse the influence of interfacial recombination between the HTM and the absorber layer, which could be investigated further. The LUMO energy level of V1236 (-2.4 eV) is considerably higher than that of P3HT (-2.8 eV) with respect to the conduction band edge (CBE) of Sb<sub>2</sub>S<sub>3</sub> (-3.4 eV). The higher difference between the CBE of Sb<sub>2</sub>S<sub>3</sub> and LUMO of V1236 results in a larger potential barrier (1 eV), which inhibits any chance of electron transport to the Au contact and thus reduces the probability of recombination compared to the P3HT case, which has a smaller energy difference (0.2 eV). The band edge alignment suggests



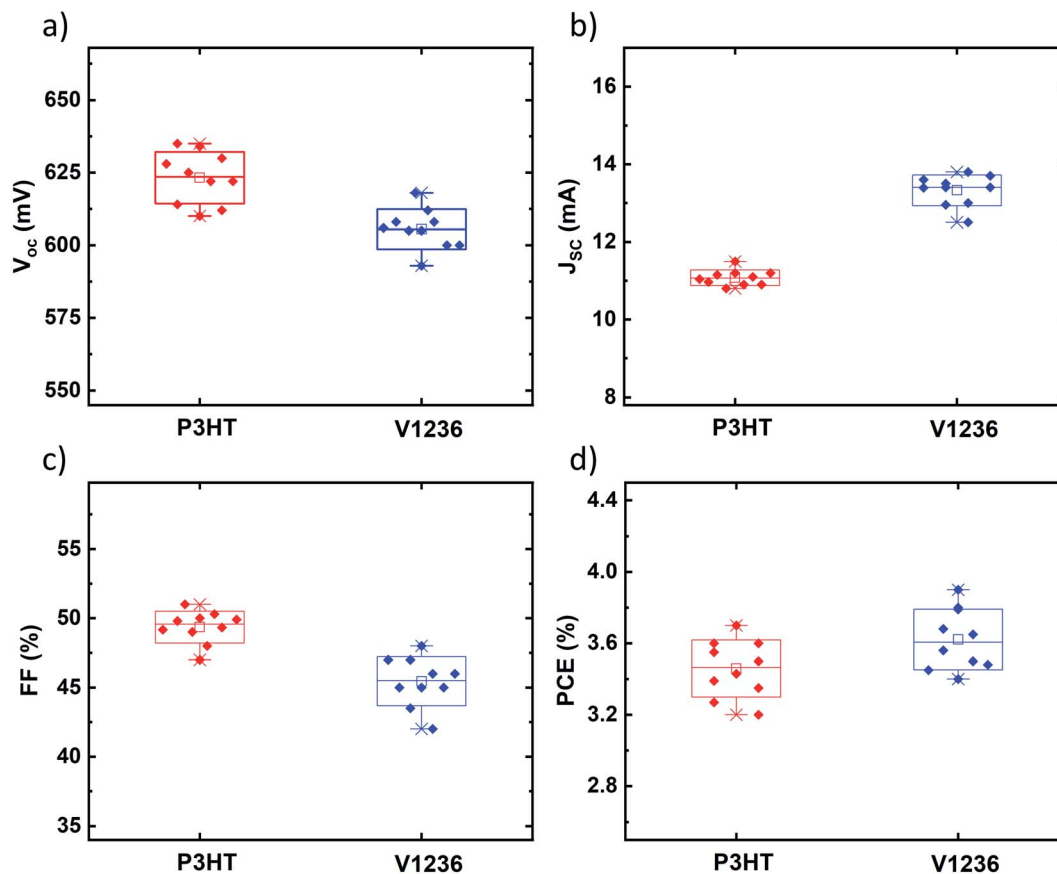


Fig. 5 Box plots showing reproducibility of (a)  $V_{OC}$ , (b)  $J_{SC}$ , (c) FF, and (d) efficiency (PCE) for champion  $Sb_2S_3$  solar cells with V1236 and P3HT as HTMs. Structure: glass/FTO/TiO<sub>2</sub>/Sb<sub>2</sub>S<sub>3</sub>/HTM/Au.

that V1236 could be a potentially more effective HTM than P3HT for  $Sb_2S_3$  solar cells.

Furthermore, the external quantum efficiencies (EQEs) of the  $Sb_2S_3$  solar cells with P3HT and V1236 are studied and the EQE curves are shown in Fig. 7a. EQE curves of solar cells with varied V1236 concentrations are shown in Fig. S8.† While the plots are amply indicative of the fact that the solar cells with V1236 have exhibited a higher spectral response in the entire wavelength

range, it may also be noted that the dip in EQE observed for P3HT devices in the 500–700 nm range is absent for V1236 devices. Overall, solar cells with V1236 have exhibited an EQE of  $\approx 80\%$  while P3HT devices have yielded 70% in the maximum absorption region, *i.e.*, 400–500 nm. Furthermore, the onset of the absorption edge is situated around 700 nm (1.8 eV), which corresponds to the bandgap of  $Sb_2S_3$  absorbers, corroborating the optical studies. The integrated  $J_{SC}$  values calculated from

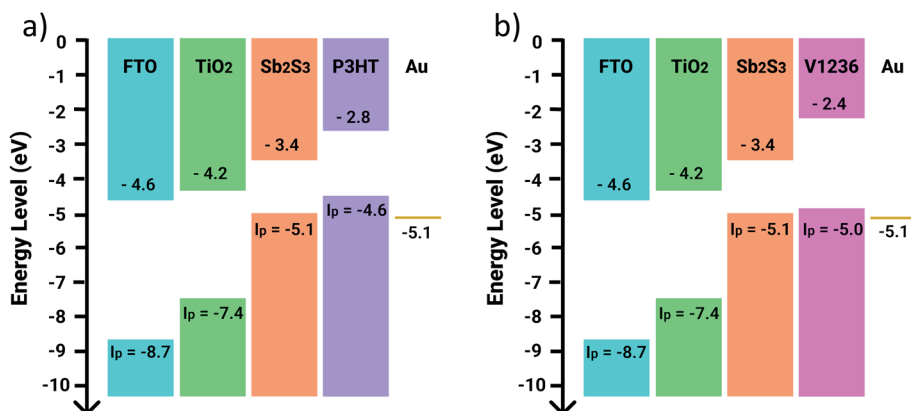


Fig. 6 Energy band diagram of  $Sb_2S_3$  solar cells with (a) P3HT and (b) V1236 as HTMs.



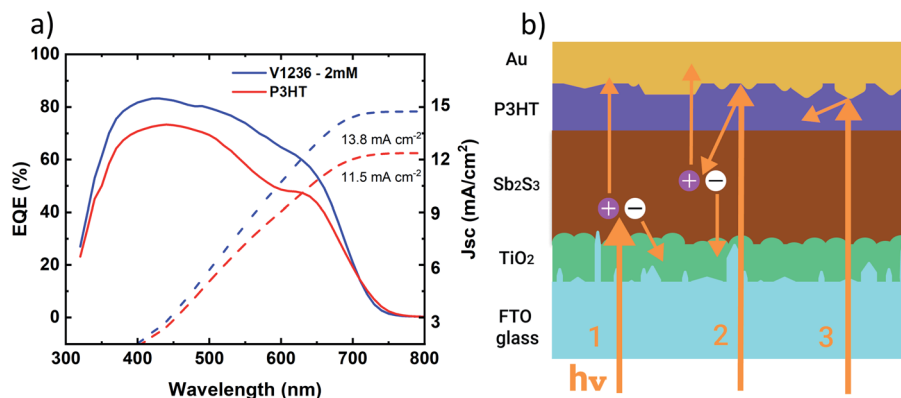


Fig. 7 (a) EQE and integrated  $J_{SC}$  of  $Sb_2S_3$  solar cells with V1236 and P3HT as HTMs and (b) schematic of the spectral response in  $Sb_2S_3$  solar cells. Structure: glass/FTO/TiO<sub>2</sub>/ $Sb_2S_3$ /HTM/Au.

EQE spectra are shown in Fig. 7a and are calculated to be 13.8 and 11.5  $\text{mA cm}^{-2}$  for V1236 and P3HT, respectively. The values are almost identical to the  $J_{SC}$  values obtained from  $J$ - $V$  characteristics (Fig. 4b). The impact of polymer-based HTMs on EQE was previously explained by Zimmermann *et al.*,<sup>27</sup> wherein three major mechanisms are held responsible. Primarily, the recombination occurs within the exciton diffusion length of the HTM while a weak electronic bonding or an unfavourable band alignment at the HTM-absorber interface also contributes to enhanced recombination and finally, parasitic absorption in the bulk of the HTM. When light traverses through the absorber, the majority of the light gets absorbed depending on the absorption co-efficient and thickness. If the thickness of the absorber is around 100 nm, some of the light transmits through and gets reflected at the HTM-metal interface, which is supposed to be reabsorbed back in the absorber. However, if the HTM is sufficiently thick ( $\approx 100$  nm), the reflected light gets absorbed within the HTM, which is responsible for parasitic absorption.<sup>27</sup> Thus, optimization of layer thicknesses, and interface modifications are key aspects in  $Sb_2S_3$ -polymer devices. The parasitic absorption coupled with the optical spacer effect of P3HT may be responsible for the overall lower EQE.<sup>27</sup> It is also known that P3HT absorbs majorly in the 500–

600 nm region due to its bandgap at 1.8 eV,<sup>3,5</sup> which further corroborates the dip seen in the EQE curve, thus attributing it to the parasitic absorption.<sup>27</sup> Furthermore, the optical spacer effect is dominant when the thickness of the absorber is less than 100 nm, which is the case in the present study. The spectral response in  $Sb_2S_3$  solar cells is schematically demonstrated in Fig. 7b, which shows the direct absorption of sun light contributing to the carrier generation (indicated as 1), the re-absorption of reflected light from the HTM-metal interface, also contributing to photogeneration (2) and the absorption of reflected light within the HTM layer (3). The spectral response in  $Sb_2S_3$  solar cells with P3HT may majorly have the phenomena 1 and 3 while V1236 devices may have 1 and 2 owing to the large difference in the thickness of HTMs, which could be witnessed from the EQE curves wherein V1236 devices displayed a larger response compared to P3HT counterparts.

To further understand the effect of spectral response, optical properties of individual HTMs coated on glass/FTO substrates are analysed and the total transmittance spectra are shown in Fig. 8a, where the reference curve is also included for the glass/FTO substrate. As can be clearly seen, the transmittance spectrum of glass/FTO/V1236 is almost identical to that of the glass/FTO sample indicating the complete transparency of the V1236

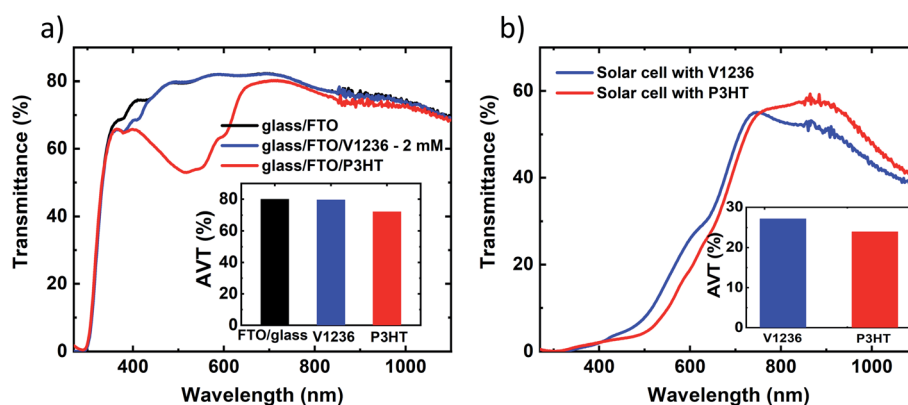
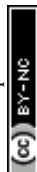


Fig. 8 Total transmission spectra of (a) glass/FTO, glass/FTO/V1236 and glass/FTO/P3HT layers and (b)  $Sb_2S_3$  solar cells with V1236 and P3HT as HTMs devoid of a back contact (insets of a and b: respective average visible transmittance bar charts in the 400–800 nm range).





HTM. P3HT, on the other hand, has exhibited a dip in the transmittance around the 500 nm region, which corresponds to the absorption within P3HT ( $E_g \approx 1.8$  eV). The solar weighted average visible transmittance (AVT) values, calculated in the 400–800 nm region, are compared as shown in the inset of Fig. 8a. The AVT for glass/FTO and glass/FTO/V1236 is almost similar around 80% while that of glass/FTO/P3HT is  $\approx 72\%$ , which further affirms that the optimized V1236 in the present study contributes to more transparency than the P3HT. Furthermore, the total transmittance spectra of V1236 at different concentrations are shown in Fig. S9,<sup>†</sup> which reveal the transparency of V1236 even for a larger thickness. It may well be noted that the thickness values of P3HT and V1236 compared herein are approximately 100 and 20 nm, respectively, which are optimized for the best efficiency  $\text{Sb}_2\text{S}_3$  in each case. Therefore, for a fair comparison of the optical properties, thinner P3HT deposited on glass/FTO, obtained by diluting the concentration, is compared with V1236 as shown in Fig. S10.<sup>†</sup> Although the thinner P3HT has exhibited enhanced transparency, the relevant absorption edge is still seen, which is majorly responsible for the reduced overall transparency. On a similar note, the total transmittance spectra are recorded for the solar cell devoid of a top metal contact for V1236 and P3HT devices as shown in Fig. 8b. While both the devices have exhibited AVT over 20%, V1236 devices have shown enhanced transparency (about 20% higher) compared to P3HT devices thereby validating the use of V1236 as an HTM in semi-transparent  $\text{Sb}_2\text{S}_3$  solar cells.

## 4 Conclusions

In conclusion, a cost-effective and transparent fluorene-based enamine (V1236) hole transport material has been successfully demonstrated, for the first time, in the fabrication of semi-transparent  $\text{Sb}_2\text{S}_3$  solar cells yielding a power conversion efficiency of 3.9% with an average visible transmission of 27% in the 400–800 nm spectral range. When compared with conventional P3HT based solar cells, the significantly cheaper V1236 devices have exhibited similar efficiencies and improved transparency. It is observed that the parasitic absorption losses coupled with absorption in the visible range exhibited by P3HT are not present in the case of V1236 thereby validating its efficacy as an HTM for semi-transparent solar cells. Furthermore, the band diagram of solar cells with P3HT and V1236 as HTMs reveals that V1236 is a more effective HTM for the  $\text{Sb}_2\text{S}_3$  absorber owing to its improved band alignment. The study, on a whole, put forward the use of new and significantly cheaper V1236 as an HTM in semi-transparent  $\text{Sb}_2\text{S}_3$  solar cells, which paves the way towards solar window applications.

## Author contributions

Nimish Juneja – conceptualization, data curation, formal analysis, methodology, validation, visualization, and writing – original draft. Sreekanth Mandati – conceptualization, investigation, formal analysis, methodology, validation, visualization, supervision, and writing – review & editing. Atanas Katerski – methodology and validation. Nicolae Spalatu – writing – review

& editing. Sarune Daskeviciute-Geguziene – methodology and writing – review & editing. Aivars Vembris – methodology and writing – review & editing. Smagul Karazhanov – writing – review & editing. Vytautas Getautis – methodology and writing – review & editing. Malle Krunkis – formal analysis, supervision, and writing – review & editing. Ilona Oja Acik – formal analysis, funding acquisition, project administration, resources, supervision, and writing – review & editing.

## Conflicts of interest

There are no conflicts to declare.

## Acknowledgements

The “Development of Semi-Transparent Bifacial Thin Film Solar Cells for Innovative Applications” benefits from a 999372 € grant from Iceland, Liechtenstein and Norway through the EEA Grants. The aim of the project is to develop a new approach based on novel materials and structures and production technologies, which are the key to further increase the share, and range of applications of PV in areas with sub-average sunlight, including Baltic and Nordic countries. Therefore, development of resource saving, cost-effective and efficient PV devices is a primary challenge of this project. Project contract with the Research Council of Lithuania (LMTLT) No is S-BMT-21-1(LT08-2-LMT-K-01-003). The Department of Materials and Environmental Technology, Tallinn University of Technology has received funding from Estonian Research Council project PRG627 “Antimony Chalcogenide Thin Films for Next-Generation Semi-Transparent Solar Cells Applicable in Electricity Producing Windows”, the Estonian Centre of Excellence project TK141 (TAR16016EK) “Advanced Materials and High-Technology Devices for Energy Recuperation Systems”, the European Union's Horizon 2020 programme under the ERA Chair project 5GSOLAR grant agreement No 952509 and PSG689 “Bismuth Chalcogenide Thin-Film Disruptive Green Solar Technology for Next Generation Photovoltaics”. Institute of Solid-State Physics, University of Latvia has received funding from the European Union's Horizon 2020 Framework Programme H2020-WIDESPREAD-01-2016-2017-Teaming Phase 2 under grant agreement No. 739508, project CAMART<sup>2</sup>. The authors thank Dr Tadas Malinauskas and Dr Valdek Mikli for their support in preparation and characterization of the samples.

## Notes and references

- 1 M. Y. Versavel and J. A. Haber, *Thin Solid Films*, 2007, **515**, 7171–7176.
- 2 S. Messina, M. T. S. Nair and P. K. Nair, *Thin Solid Films*, 2007, **515**, 5777–5782.
- 3 J. S. Eensalu, A. Katerski, E. Kärber, L. Weinhardt, M. Blum, C. Heske, W. Yang, I. Oja Acik and M. Krunkis, *Beilstein J. Nanotechnol.*, 2019, **10**, 2396–2409.
- 4 R. Kondrotas, C. Chen and J. Tang, *Joule*, 2018, **2**, 857–878.



- 5 J. S. Eensalu, A. Katerski, E. Kärber, I. Oja Acik, A. Mere and M. Krunks, *Beilstein J. Nanotechnol.*, 2019, **10**, 198–210.
- 6 Y. Itzhaik, O. Niitsoo, M. Page and G. Hodes, *J. Phys. Chem. C*, 2009, **113**, 4254–4256.
- 7 Y. C. Choi, D. U. Lee, J. H. Noh, E. K. Kim and S. il Seok, *Adv. Funct. Mater.*, 2014, **24**, 3587–3592.
- 8 Y. C. Choi and S. il Seok, *Adv. Funct. Mater.*, 2015, **25**, 2892–2898.
- 9 P. Sun, M. Zhang, C. Ai, Z. Wu, S. Lu, X. Zhang, N. Huang, Y. Sun and X. Sun, *J. Power Sources*, 2016, **319**, 219–226.
- 10 H. Wedemeyer, J. Michels, R. Chmielowski, S. Bourdais, T. Muto, M. Sugiura, G. Dennler and J. Bachmann, *Energy Environ. Sci.*, 2013, **6**, 67–71.
- 11 H.-J. Jo, S. H. Kim, J. S. Kim, S.-J. Lee and D.-H. Kim, *J. Korean Phys. Soc.*, 2016, **69**, 541–546.
- 12 R. Parize, A. Katerski, I. Gromyko, L. Rapenne, H. Roussel, E. Kärber, E. Appert, M. Krunks and V. Consonni, *J. Phys. Chem. C*, 2017, **121**, 9672–9680.
- 13 N. Spalatu, R. Krautmann, A. Katerski, E. Karber, R. Josepson, J. Hiie, I. O. Acik and M. Krunks, *Sol. Energy Mater. Sol. Cells*, 2021, **225**, 111045.
- 14 R. Krautmann, N. Spalatu, R. Gunder, D. Abou-Ras, T. Unold, S. Schorr, M. Krunks and I. Oja Acik, *Sol. Energy*, 2021, **225**, 494–500.
- 15 C. P. Liu, H. E. Wang, T. W. Ng, Z. H. Chen, W. F. Zhang, C. Yan, Y. B. Tang, I. Bello, L. Martinu, W. J. Zhang and S. K. Jha, *Phys. Status Solidi B*, 2012, **249**, 627–633.
- 16 N. Ali, A. Hussain, R. Ahmed, W. N. W. Shamsuri, A. Shaari, N. Ahmad and S. M. Abbas, *Appl. Phys. A: Solids Surf.*, 2016, **122**, 23.
- 17 M. I. Medina-Montes, Z. Montiel-González, N. R. Mathews and X. Mathew, *J. Phys. Chem. Solids*, 2017, **111**, 182–189.
- 18 Y. Zeng, F. Liu, M. Green and X. Hao, in *2018 IEEE 7th World Conference on Photovoltaic Energy Conversion (WCPEC) (A Joint Conference of 45th IEEE PVSC, 28th PVSEC & 34th EU PVSEC)*, IEEE, 2018, pp. 0870–0872.
- 19 L. Guo, B. Zhang, S. Li, Q. Zhang, M. Buettner, L. Li, X. Qian and F. Yan, *APL Mater.*, 2019, **7**, 041105.
- 20 W. Lian, C. Jiang, Y. Yin, R. Tang, G. Li, L. Zhang, B. Che and T. Chen, *Nat. Commun.*, 2021, **12**, 3260.
- 21 C. Lan, G. Liang, H. Lan, H. Peng, Z. Su, D. Zhang, H. Sun, J. Luo and P. Fan, *Phys. Status Solidi RRL*, 2018, **12**, 1800025.
- 22 M. S. You, C.-S. Lim, D. H. Kwon, J. H. Heo, S. H. Im and K. J. Chae, *Org. Electron.*, 2015, **21**, 155–159.
- 23 D.-H. Kim, S.-J. Lee, M. S. Park, J.-K. Kang, J. H. Heo, S. H. Im and S.-J. Sung, *Nanoscale*, 2014, **6**, 14549–14554.
- 24 Y. Zhang, S. Li, R. Tang, X. Wang, C. Chen, W. Lian, C. Zhu and T. Chen, *Energy Technol.*, 2018, **6**, 2126–2131.
- 25 J. Chen, J. Qi, R. Liu, X. Zhu, Z. Wan, Q. Zhao, S. Tao, C. Dong, G. Y. Ashebir, W. Chen, R. Peng, F. Zhang, S. Yang, X. Tian and M. Wang, *Commun. Chem.*, 2019, **2**, 121.
- 26 E. Kärber, A. Katerski, I. Oja Acik, A. Mere, V. Mikli and M. Krunks, *Beilstein J. Nanotechnol.*, 2016, **7**, 1662–1673.
- 27 E. Zimmermann, T. Pfadler, J. Kalb, J. A. Dorman, D. Sommer, G. Hahn, J. Weickert and L. Schmidt-Mende, *Adv. Sci.*, 2015, **2**, 1500059.
- 28 H. Lei, G. Yang, Y. Guo, L. Xiong, P. Qin, X. Dai, X. Zheng, W. Ke, H. Tao, Z. Chen, B. Li and G. Fang, *Phys. Chem. Chem. Phys.*, 2016, **18**, 16436–16443.
- 29 T. Malinauskas, M. Saliba, T. Matsui, M. Daskeviciene, S. Urnikaite, P. Gratia, R. Send, H. Wonneberger, I. Bruder, M. Graetzel, V. Getautis and M. K. Nazeeruddin, *Energy Environ. Sci.*, 2016, **9**, 1681–1686.
- 30 S. H. Im, C.-S. Lim, J. A. Chang, Y. H. Lee, N. Maiti, H.-J. Kim, Md. K. Nazeeruddin, M. Grätzel and S. il Seok, *Nano Lett.*, 2011, **11**, 4789–4793.
- 31 X. Jin, Y. Yuan, C. Jiang, H. Ju, G. Jiang, W. Liu, C. Zhu and T. Chen, *Sol. Energy Mater. Sol. Cells*, 2018, **185**, 542–548.
- 32 L. Zhang, C. Jiang, C. Wu, H. Ju, G. Jiang, W. Liu, C. Zhu and T. Chen, *ACS Appl. Mater. Interfaces*, 2018, **10**, 27098–27105.
- 33 A. Shit, P. Chal and A. K. Nandi, *Phys. Chem. Chem. Phys.*, 2018, **20**, 15890–15900.
- 34 S. Daskeviciute, C. Momblona, K. Rakstys, A. A. Sutanto, M. Daskeviciene, V. Jankauskas, A. Gruodis, G. Bubniene, V. Getautis and M. K. Nazeeruddin, *J. Mater. Chem. A*, 2021, **9**, 301–309.
- 35 M. L. Petrus, T. Bein, T. J. Dingemans and P. Docampo, *J. Mater. Chem. A*, 2015, **3**, 12159–12162.
- 36 F. Machui, M. Hösel, N. Li, G. D. Spyropoulos, T. Ameri, R. R. Søndergaard, M. Jørgensen, A. Scheel, D. Gaiser, K. Kreul, D. Lenssen, M. Legros, N. Lemaitre, M. Vilkmann, M. Välimäki, S. Nordman, C. J. Brabec and F. C. Krebs, *Energy Environ. Sci.*, 2014, **7**, 2792.
- 37 J. Latvels, R. Grzibovskis, K. Pudzs, A. Vembris, D. Blumberga, B. P. Rand, C. Adachi, D. Cheyons and V. van Elsbergen, *J. Mater. Chem. C*, 2014, 91371G.

